 CMES, vol.80, no.1, pp.23-56, 2011

Atomistic Exploration of Deformation Properties of Copper Nanowires with Pre-Existing Defects

H.F. Zhan and Y.T. Gu[1]

Abstract: Based on the embedded atom method (EAM) and molecular dynamics (MD) method, in this paper, the tensile deformation properties of Cu nanowires (NWs) with different pre-existing defects, including single surface defects, surface bi-defects and single internal defects, are systematically studied. In-depth deformation mechanisms of NWs with pre-existing defects are also explored. It is found that Young's modulus is insensitive to different pre-existing defects, but yield strength shows an obvious decrease. Defects are observed influencing greatly on NWs' tensile deformation mechanisms, and playing a role of dislocation sources. Besides of the traditional deformation process dominated by the nucleation and propagation of partial dislocations, the generations of twins, grain boundaries, five-fold deformation twins, hexagonal close-packed (HCP) structure and phase transformation from face-centred cubic (FCC) structure to HCP structure have been triggered by pre-existing defects. It is found that surface defect intends to induce larger influence to yield strength than internal defect. Most importantly, the defect that lies on slip planes exerts larger influence than other defects. As expected, it is also found that the more or longer of the defect, the bigger influence will be induced.

Keywords: nanowire, defect, deformation mechanism, molecular dynamics, tension

1 Introduction

As one type of the most exciting nanomaterials, nanowires (NWs) have become the focus of intensive research, owing to their distinct mechanical, electrical, optical and other properties that arise from their nanometre size scale and possible quantum confinement [Sarkar, Khan and Basumallick 2007; Xia, Yang, Sun, Wu, Mayers, Gates, Yin, Kim and Yan 2003]. NWs are widely used as the active com-

[1] School of Engineering Systems, Queensland University of Technology, Brisbane, QLD 4001, Australia

ponents of nanoelectromechanical systems (NEMS) including high frequency resonator [Husain, Hone, Postma, Huang, Drake, Barbic, Scherer and Roukes 2003; Li, Mayer, Sioss, Keating and Bhiladvala 2007], force and pressure sensing [Rugar, Budakian, Mamin and Chui 2004], ultrahigh-resolution mass sensing [Yang, Callegari, Feng, Ekinci and Roukes 2006], and other devices [Ekinci and Roukes 2005]. To investigate the revolutionary characteristics of NWs usually relies on a variety of experimental approaches such as the atomic force microscope (AFM)-based bending and nanoindentation [Heidelberg, Ngo, Wu, Phillips, Sharma, Kamins, Sader and Boland 2006; Hoffmann, Utke, Moser, Michler, Christiansen, Schmidt, Senz, Werner, Gösele and Ballif 2006; Ni and Li 2006]. Recent tensile experimental study [Yue, Liu, Zhang, Han and Ma 2011] suggests that the elastic strain achievable in Cu NWs increases with the decrease of the sample diameter, which approached the 'smaller is stronger and more elastic' trend predicted by molecular dynamics (MD) simulations and *ab initio* calculations. Although, the experimental approaches can provide meaningful information on the properties of NWs, due to the extremely small dimensions of NWs, experiments are facing with huge challenges. For example, during bending experiments, the holding of NWs onto the test setup or the precise placement of the tip on NWs would be very sophisticated and difficult [Yan, Zhang, Sun, Fei, Liang and Dong 2008]. Particularly, experimental studies do not allow us to explore the in-depth deformation mechanisms underlying the deformation phenomena.

Because of the experimental deficiency, the numerical study of NWs' properties has received widespread attention, such as *ab initio* calculations, MD simulations and multi-scale simulations [Ghoniem and Cho 2002]. For example, serial MD studies of Au NWs have been carried out, regarding to the broken phenomenon, strain rates effect, temperature effect and size effect under tensile deformation [Da Silva, da Silva and Fazzio 2001; Diao and Gall 2004; Gall, Diao and Dunn 2004; Park and Zimmerman 2005]. Considering the versatile potential applications of NWs, MD investigations of NWs' mechanical behaviours under different loading conditions have been considered, e.g. bending deformation [Chan, Luo and Zhang 2008; Chen and Zhu 2007; McDowell, Leach and Gall 2008], compression [Jiang and Batra 2009; Olsson and Park 2011] and torsion [Jiang, Zhang, Zheng and Chen 2009; Weinberger and Cai 2010]. As is well known, NWs possess a significant surface-to-volume ratio, leading to a plethora of novel mechanical behaviours originating from the surface effects. To date, MD simulations have unveiled the phase transformations [Diao, Gall and Dunn 2003], pseudoelastic behaviour [Park, Gall and Zimmerman 2005] and shape memory [Liang, Zhou and Ke 2005; Park and Ji 2006] of NWs. In the meanwhile, some multi-scale simulations [Park and Klein 2007; Park, Klein and Wagner 2006] and theoretical calculations [He and Lilley

2008; Wang and Feng 2007] have also been conducted to incorporate the surface effect to NWs' properties.

As materials used in the real engineering always contain imperfections, which might be induced during the fabrication or manufacturing processes, e.g. impurity, grain boundary (GB), surface defects, nano-cavities and others. Recent work conducted by Sansoz et al. [Sansoz, Huang and Warner 2008] revealed that, twin boundaries (TBs) are ubiquitous for both synthesis and properties in nano-enhanced FCC metals. By using MD simulations, Chen et al. [Chen, Xiao, Chen and Wu 2010] reported that, during the machining and stretching of single crystal Cu, stacking faults (SFs) will be generated inside the specimen, which will greatly affect the specimen's properties under tension. Kuramoto et al. [Kuramoto, Ohsawa and Tsutsumi 2002] investigated the fundamental behaviours of point defects, clusters and interaction with dislocation in Fe and Ni crystal by computer simulation. Besides of loading conditions and morphologies, Zhang et al. [Zhang, Huang and Atluri 2008] reported that the strength of NWs also depends on the twin spacing. Due to the nanometre size scale, the presence of defects is considered as one of the most influential factors in determining NWs' properties. Experimental study [Wu, Heidelberg, Boland, Sader, Sun and Li 2006] demonstrates that, NWs' mechanical properties could be uniquely tailored by controlling their structure (through assembling materials with oriented, interlocking grains). It is seen that, studying the defect's effect is crucial to enhance the utility of NWs. Unfortunately, the nanoscale defects are difficult to detect [Higgins, Bout, Kerimo and Barbara 1996]. The imaging techniques are limited at the atomic size scale, and the lack of proper analytical methods has greatly impeded the investigations of defects [Ishigami, Choi, Aloni, Louie, Cohen and Zettl 2004]. Even if we have a technique to identify the nanoscale defect, currently, it is still extremely hard or even impossible to prepare or control a sample with a designed defect for a specific experimental study. Therefore, considering the significant difficulties that experimental study of the defect's effect encounters, we can expect the MD simulation plays a critical role for it. However, comparing with the abundant MD studies of perfect NWs, only few researches are found investigating the defected NWs. Recently, a serial MD studies of TBs effect to NWs' properties have been reported [Cao and Wei 2006; Cao, Wei and Mao 2007; Deng and Sansoz 2009; Deng and Sansoz 2009]. Zhang and Huang [Zhang and Huang 2009] suggested that whether TBs strengthen NWs depends on the surface morphologies. Particularly, TBs would soften NWs if they have circular cross-section or strength NWs when they have square cross-section. To the best of author's knowledge, there is still no systematic MD study of the pre-existing defect's effect on NWs' properties. This topic calls for a significant development.

Our preliminary work [Zhan, Gu et al. 2011] has found the existing defect will

affect the mechanical properties (Young's modulus, yield strength) for NW's and nanomaterial in nano-indentation. Our following work [Zhan, Gu, Yan, et al. 2011] is then focused on 45° surface defects and carried out detailed investigations of the tensile deformation of Cu NWs with no periodic boundary condition. We found that, for perfect NW, the decrease regions of the stress are accompanied with SFs' generation and migration activities, but during stress increase regions, the structure of the NW appears almost unchanged. Such phenomena were also observed for the defected NW with a 45° surface defect, and the surface defect was observed exerting obvious influence to the NW's plastic deformation.

However, there are many possibilities of pre-existing defects in a NW including different orientations (different angles not only 45°), different locations (surface or internal), different sizes, and multiple defects. Different defected cases will be with different influences for different deformation mechanisms. To date, there is no systematic study for these cases. Therefore, to establish a more complete investigation of different pre-existing defect's effect, in this work, we will utilize MD simulation to investigate the deformation mechanism of Cu NWs with different pre-existing defects under tensile deformation. The Larger-scale Atomic/Molecular Massively Parallel Simulator (LAMMPS) [Plimpton, Crozier and Thompson 2007] will be employed to carry out the simulation. Note that, the surface defect that we considered in the work is similar to the surface notch investigated by Doyama [Doyama 1995] and Tyagi et al. [Tyagi, Lee, Buxton and Balazs 2004], or the defect of vacancies studied by Chang [Chang 2003]. Particularly, different pre-existing defects, including single surface defects, surface bi-defects and single internal defects have been considered. In addition, the influences of defect size and quantity have also been investigated. All simulation models studied in this paper are summarised in the Appendix.

2 Numerical implementation

2.1 Molecular dynamics simulation

MD simulations are carried out on single-crystal Cu NW under the tensile deformation. The square cross-section NW which is obtained by cutting from the bulk single-crystal Cu has been considered, with the initial atomic configuration positioned at the FCC lattice site, and the x, y, z coordinate axes represent the lattice direction of [100],[010],[001], respectively. The size of the specimen is $6a \times 6a \times 30a$, where a is the Cu lattice constant, and the value of 3.615 Å is applied. Periodic boundary condition is applied in z direction with the other two directions of free surfaces. The NW is first relaxed to a minimum energy state at 0 K using conjugate gradient energy minimization and then the Nose-Hoover thermostat [Hoover

1985; Nosé 1984] is employed to equilibrate the NW at an approximate zero temperature, namely 0.01 K. As reported by previous researchers [Ikeda, Qi, Çagin, Samwer, Johnson and Goddard 1999], at high strain rate (>10^{10} s^{-1}), the metal NW will transform to an amorphous state and undergo homogeneous deformation flow. To avoid such a deformation process, a constant strain rate of $5\times10^{8}s^{-1}$ will be applied. During the simulation, the temperature of the system is kept at 0.01 K by a velocity rescaling algorithm. The following embedded atom method (EAM) potential [Daw and Baskes 1984] developed for Cu by Mishin [Mishin, Mehl, Papaconstantopoulos, Voter and Kress 2001] is used to describe the atomic interactions during these simulations.

$$E_{tot} = \sum_i F(\rho_i) + \frac{1}{2}\sum_i \sum_j V(r_{ij}), \rho_i = \sum_j \Phi(r_{ij}) \tag{1}$$

Here V, F, ρ are the pair potential, the embedded energy, and the electron cloud density, respectively. i and j are the number of atoms, and r_{ij} is the distance between them. This potential is chosen as it could reliably predict the material SFs energies and the stability of nonequilibrium structures of Cu. The equations of motion are integrated with time using a Velocity Verlet algorithm [Plimpton 1995]. The above simulation settings will be employed in all following simulations without further declaration. In order to analyse the partial dislocation and SFs during the tensile deformation, the centro-symmetry parameter (*csp*) is used [Kelchner, Plimpton and Hamilton 1998; Van Swygenhoven and Derlet 2008], which is defined as follows:

$$csp = \sum_{i=1,6} \left| \vec{R}_i + \vec{R}_{i+6} \right|^2 \tag{2}$$

where $\vec{R}_i$ and $\vec{R}_{i+6}$ are the vectors corresponding to the six pairs of opposite nearest neighbours in FCC lattice. The *csp* value increases from 0 for perfect FCC lattice to positive values for defects and for atoms close to free surfaces. During this work, $0.5 < csp \leq 3$, $3 < csp \leq 12$, and $csp > 12$ are assigned to identify the partial dislocations, SFs and surface atoms, respectively. According to the *csp* definition, intrinsic SF will have two adjacent SF layers, and for extrinsic SF or twins, two translated SF layers will be observed with atoms between these two layers still in FCC environment.

2.2 Perfect NW

As no experimental result is available for a NW with a specific defect, for validation and comparison, we first study a perfect Cu NW under tension which has been

frequently discussed by previous researchers [Koh and Lee 2006; Koh, Lee, Lu and Cheng 2005; Liang and Zhou 2003; Sutrakar and Mahapatra 2009]. According to the definition of yield strength in continuum mechanics and the atomic configurations during simulation, *we refer yield strength as the stress when partial dislocations first emitted, and the corresponding strain is taken as yield strain.* Specifically, the engineering strain is used in this work, which is defined as: $\varepsilon = (l - l_0)/l_0$. Here, l is the instantaneous length and l_0 is the initial length of the NW after the energy minimization.

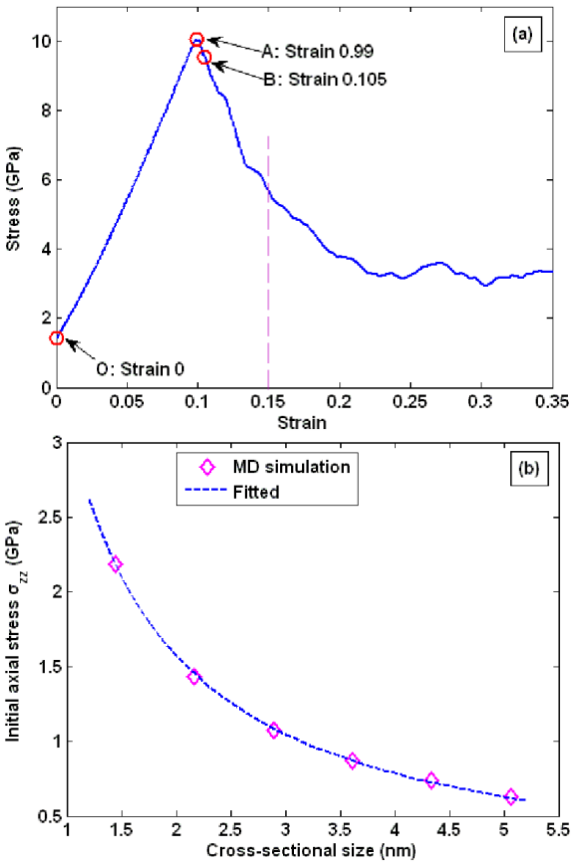

Figure 1: (a) Stress-strain curve of perfect Cu NW during tensile deformation; (b) Initial stress versus cross-sectional size.

Figure 1(a) shows the stress-strain curve of a perfect NW under tension. From this figure, we notice that the initial stress (i.e. when strain is zero) of the NW is

1.423 *GPa*, not zero. This non-zero initial stress in NW has also been reported by Liang and Zhou [Liang and Zhou 2004], and they reported a value around 0.4∼1.6 *GPa*, which is agreed with our result. Actually, such a non-zero initial stress is believed resulting from the effect of surface stresses. This assumption is easy to prove by setting the simulation model with periodic boundary conditions in all three dimensions (x, y and z). It likes a simulation of a bulk material, and our simulation has obtained the initial stress is around zero due to no surface stress existed. Further investigation of the surface stress effect has been conducted as below. We consider six groups of NWs with cross-sectional size as $4a$, $6a$, $8a$, $10a$, $12a$, $14a$, and the length of all NWs in these six groups as $30a$. Energy minimization process is performed for all NWs under the same minimization criterion. Namely, the change in total energy between two adjacent iterations divided by the initial total energy is less than or equal to the tolerance 10^{-8}. The initial axial stress σ_{zz} estimated from the simulation is plotted in figure 1(b), in which σ_{zz} is found decreasing with the increase of cross-sectional size d. By employing the least square fitting procedure, we find the relation between σ_{zz} and d is well described by the inverse proportional function, i.e.,

$$\sigma_{zz} = 3.144/d \tag{3}$$

In fact, Diao et al. [Diao, Gall and Dunn 2004] proposed that, for <100> NWs with square cross-section, the initial axial stress that originated from surface stress can be estimated as:

$$\sigma_{zz} = 4fd/A = 4f/d \tag{4}$$

where f is the surface stress and A is the cross-section area by supposing $A = d^2$. Comparing (3) and (4), we can obtain the (100) surface stress $f = 3.144/4 = 0.786$ $J{\cdot}m^{-2}$ for the Cu NW, which is very close to the value reported by Streitz et al. [Streitz, Cammarata and Sieradzki 1994] as 0.896 $J{\cdot}m^{-2}$. Note that, researchers found the surface stress is tensile for FCC metals [Wan, Fan, Gong, Shen and Fan 1999], but compressive for semiconductor NWs [Shim, Zhou, Huang and Cale 2005].

According to figure 1(a), point 'A' of the stress-strain curve is observed as the yield point. Before yielding, an approximately linear region (region O∼A) is found, which is consistent with the tensile experiments as an elastic deformation process. Young's modulus determined from the stress-strain curve with the strain <3% using linear regression is 75.188 *GPa*, and the estimated yield strength is 10.06 *GPa*. These results are agreed with the values reported by other researchers [Ji and Park 2007; Liang and Zhou 2004; Wu 2006]. After yielding, the stress shows a continuous decrease. In particular, at the beginning of yielding during the region of

A∼B, only atoms located around the NW's four edges are found experiencing a slight offset from the perfect lattice, as illustrated in figure 2(a). Such phenomenon is also reported by Huang et al. [Huang, Zhang and Guo 2006] when they investigated the deformation of Fe and Ni NWs. After the strain passing point 'B', we find a $[1\bar{1}2](1\bar{1}\bar{1})/6$ partial dislocation emitted from one of the NW's edges, as illustrated in figure 2(b). With further elongation, the existences of both the intrinsic and extrinsic SFs are observed (figure 2(c)). A single necking area is found located around the middle of the NW at the strain of 0.6 (figure 2(d)). According to Koh and Lee [Koh and Lee 2006], the location of necking is supposed highly related to the strain rate, which could be predicted by the longitudinal wave propagation equation. In all, the atomic configures in figure 2 suggest that, the tensile deformation of a perfect Cu NW is dominated by the nucleation and propagation of partial dislocations (slip dominated deformation process), which is consistent with conclusions by previous researchers [Diao, Gall, Dunn and Zimmerman 2006; Park, Gall and Zimmerman 2006].

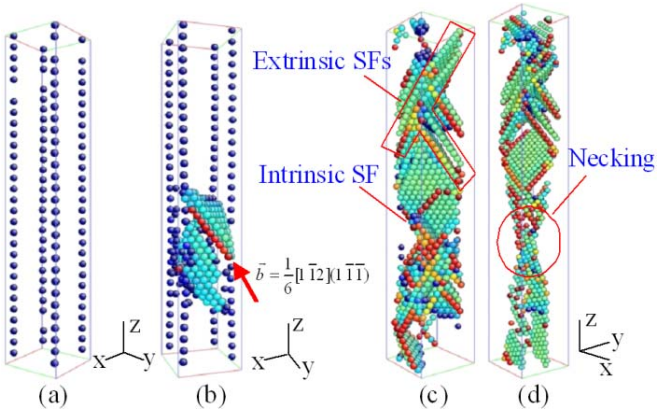

Figure 2: Atomic configurations of perfect Cu NW at different strain points: (a) Strain 0.10; (b) Strain 0.109; (c) Strain 0.2; (d) Strain 0.6. For all figures, only atoms with the textitcsp value between 0.5 and 12 are visualized.

3 Deformation mechanism analysis of NWs with pre-existing defects

3.1 NW with different pre-existing single surface defects

Cu NWs with five different pre-existing single surface defects are considered first, with the size chosen as $6a\times6a\times30a$. Simulation models are shown in figure 3, including: Case I: with surface horizon defect; Case II: with surface vertical defect;

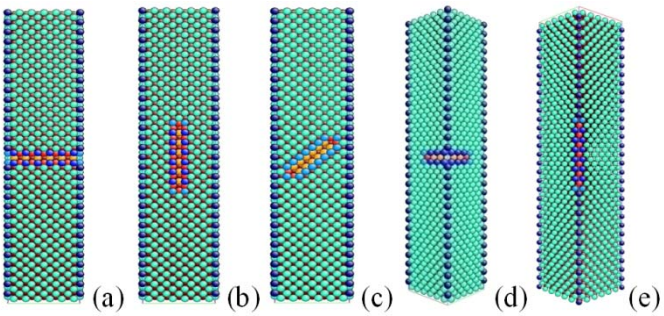

Figure 3: NWs with different pre-existing single surface defects: (a) Case I: with surface horizon defect; (b) Case II: with surface vertical defect; (c) Case III: with surface 45° defect; (d) Case IV: with surface corner defect; (e) Case V: with surface edge defect.

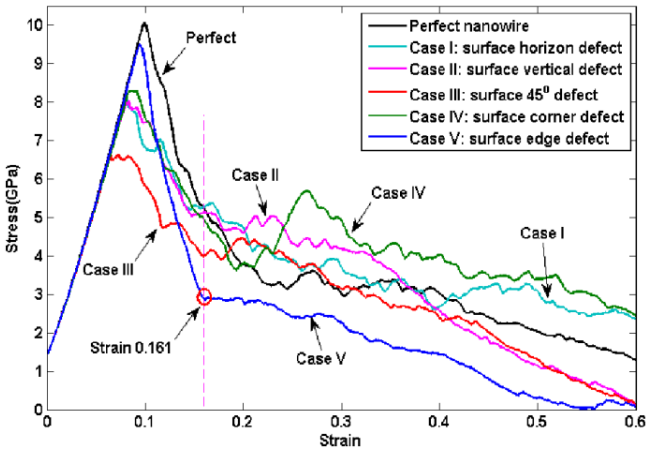

Figure 4: Stress-strain curves of NWs with different preexisting single surface defects.

Case III: with surface 45° defect; Case IV: with surface corner defect; Case V: with surface edge defect. Different surface defects are generated by removing the same amount of atoms according to different positions and orientations on the NWs' surface.

Figure 4 shows the stress-strain curves of NWs with different single surface defects, as well as the perfect NW. Firstly, we find the elastic regions of these stress-strain curves are almost coincident with each other. By applying linear regression to the stress-strain curves with the strain <3%, Young's modulus is observed almost

the same for all five defected NWs. Comparing with the perfect NW, the largest decrease of the estimated Young's modulus is only about 1.25% in Case III. Such small decrease indicates that Young's modulus is insensitive to the pre-existing surface defects. A similar result has been found by Zhao et al. [Zhao, Chen, Shen and Lu 2009], i.e. Young's modulus is independent of the nano-void in a periodic unit cell subjected to the uniaxial tension. However, an earlier study undertaken by Chang [Chang 2003] revealed that Young's modulus decreases with the increase of the vacancy fraction. Such discrepancy is expected resulting from the Lennard-Jones (L-J) potential that being employed, as the L-J potential is supposed to have significant problems when the local environment is substantially different from the uniform bulk, such as surfaces, GBs, internal voids, and fracture process [Foiles, Baskes and Daw 1986].

Secondly, an obvious decrease of yield strength and yield strain is observed due to the surface defect. The largest decrease is observed in Case III with the surface 45^o defect, and the smallest decrease is found in Case V with the surface edge defect. Thirdly, obvious different plastic deformation processes are found for different cases. As illustrated in figure 4, different stress fluctuations are observed in the stress-strain curves. The related deformation process is discussed as follows.

Figure 5 shows the atomic configurations of Case I with surface horizon defect at strains of 0.084, 0.2 and 0.6. At the beginning of yielding, four leading partial dislocations are initially emitted from two ends of the surface horizon defect and propagate into the interior, as pointed out in figure 5(a). With further elongation, the formations of extrinsic SFs are observed. Especially, we find a twin is developed due to the further slip of an extrinsic SF at the strain of 0.2. The transitions between extrinsic SF and twins are observed following the increase of strain. Interestingly, when the strain reaches 0.6, a fraction of the NW with four adjacent SF layers is found, as illustrated in figure 5(c). Based on the *csp* definition given in (2), such structures indicate the formation of hexagonal close-packed (HCP) structure. As the HCP structure is also observed in NWs with other defects, thus, more detail explanations are provided later. It is worth to mention that, two obvious twins are observed at the strain of 0.6. Close inspection reveals that, the twinning process has resulted in the exposure of low energy $\{111\}$ surfaces on the part between two twin boundaries (TBs), rather than the original $\{100\}$ surfaces. Furthermore, the necking is found located at the end of the NW. This is acceptable when the NW is having periodic boundary conditions in the axial direction.

Figure 6 presents the atomic configurations of Case II with surface vertical defect at strains of 0.09, 0.2 and 0.6. Different from Case I, only two leading partial dislocations are initially emitted around the surface defect, as shown in figure 6(a). At the strain of 0.2, only the existences of intrinsic SF and extrinsic SF are observed.

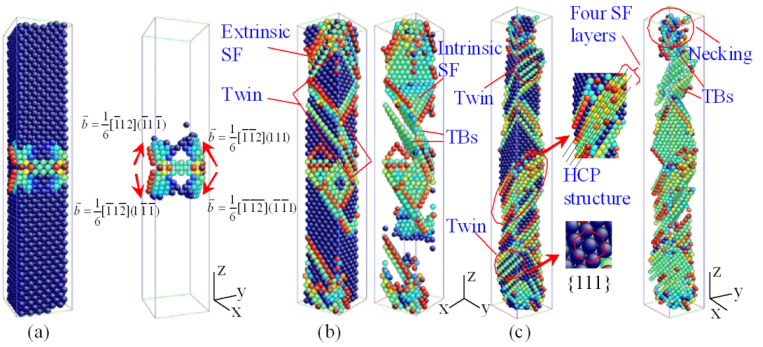

Figure 5: Atomic configurations of Case I with surface horizon defect: (a) Strain 0.084; (b) Strain 0.2; (c) Strain 0.6. Two figures are provided at each strain point, and atoms with *csp* value between 0 and 12, 0.5 and 12 are visualized in the left and right figure, respectively.

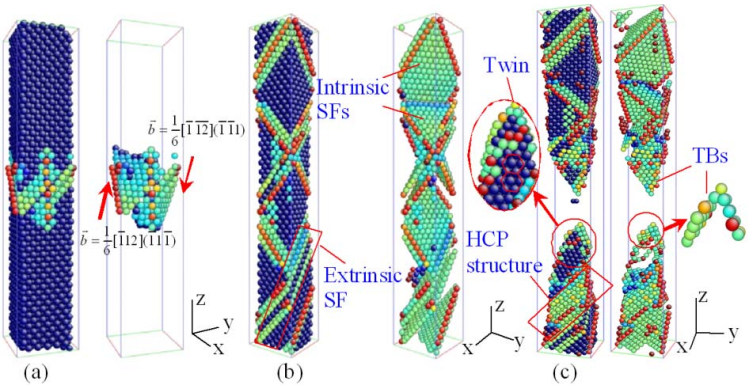

Figure 6: Atomic configurations of Case II with surface vertical defect: (a) Strain 0.09; (b) Strain 0.2; (c) Strain 0.6. Two figures are provided at each strain point, and atoms with *csp* value between 0 and 12, 0.5 and 12 are visualized in the left and right figure, respectively.

The NW is found already fractured at the strain of 0.6 with an obvious fraction deformed into a HCP structure. It is observed that, the necking area undergoes a great deal of nucleation and propagation activities of partial dislocations. Specifically, the crystal structure in the necking area is seriously distorted first, and then rearrangement happened. As illustrated in figure 6(c), this rearrangement makes the exposure surfaces at the fracture region as low energy {111} surfaces, indicating the formation of twins.

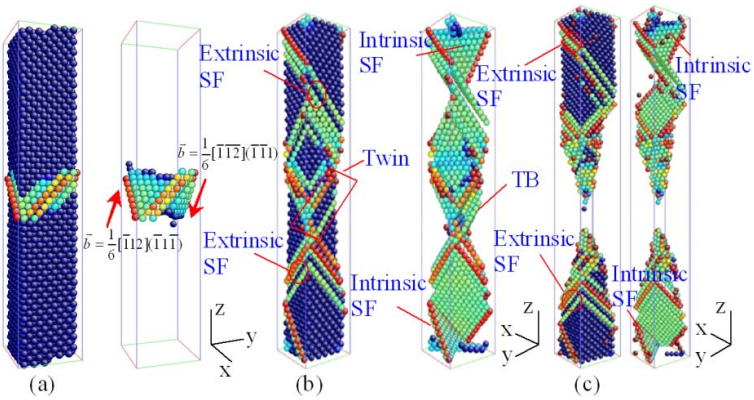

Figure 7: Atomic configurations of Case III with surface 45o defect: (a) Strain 0.068; (b) Strain 0.2; (c) Strain 0.6. Two figures are provided at each strain point, and atoms with *csp* value between 0 and 12, 0.5 and 12 are visualized in the left and right figure, respectively.

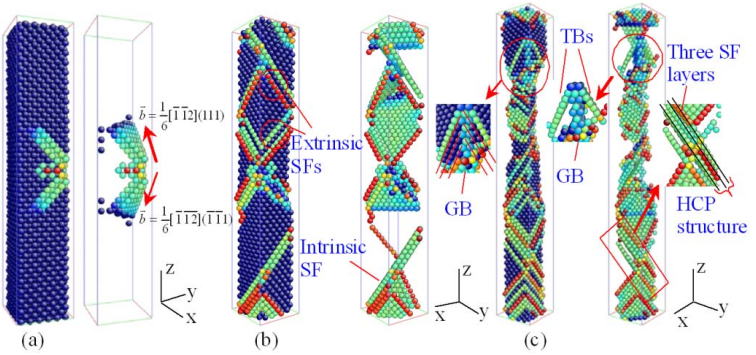

Figure 8: Atomic configurations of Case IV with surface corner defect: (a) Strain 0.084; (b) Strain 0.2; (c) Strain 0.6. Two figures are provided at each strain point, and atoms with *csp* value between 0 and 12, 0.5 and 12 are visualized in the left and right figure, respectively.

Figure 7 reveals the atomic configurations of Case III with surface 45˚ defect at strains of 0.068, 0.2 and 0.6. As indicated by the stress-strain curve in figure 4, we find an early yielding of the NW with two leading partial dislocations emitted around the surface defect at the strain of 0.068. With the increase of strain, the formation of extrinsic SF is observed, as well as the generation of twins around the middle of the NW. From figure 7(b), we find the NW has a similar deformed

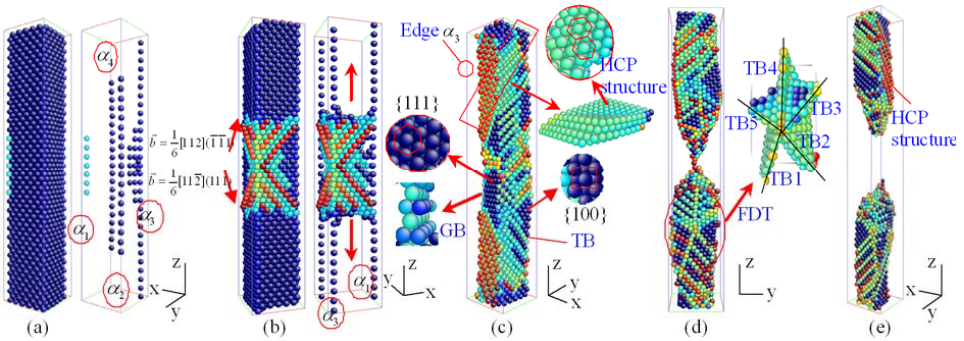

Figure 9: Atomic configurations of Case V with surface edge defect: (a) Strain 0.084; (b) Strain 0.105; (c) Strain 0.161; (d) Strain 0.422; (e) Strain 0.6. For the right figure of (a) and (b), atoms with *csp* value between 0.5 and 12 are visualized; others, atoms with *csp* value between 0 and 12 are viewed.

structure at two ends, with one intrinsic SF intersected with one extrinsic SF. It is interested to find that, this similar structure is retained even when the NW is fractured at the strain of 0.6. Such phenomenon suggests that the 45° defect has greatly reduced the strength of the domain where the defect locates at, leading most of the deformation activities concentrated around the middle of the NW. Note that, the existences of twins are observed only within a very short duration, and they are found deformed into extrinsic SFs. According to figure 7(c), besides of the intrinsic SFs and extrinsic SFs, the exposure surfaces of the NW are the original {100} surfaces. Hence, it could be concluded that the dominate deformation process is the nucleation and propagation of partial dislocations.

Figure 8 shows the atomic configurations of Case IV with surface corner defect at strains of 0.084, 0.2 and 0.6. Basically, two leading partial dislocations are firstly emitted around the surface defect when yielding occurs, as pointed out in figure 8(a). Along with the increment of elongation, we find the transitions between intrinsic SF and extrinsic SF. At the strain of 0.6, an apparent necking area is developed. Within this region, we find the existence of a grain boundary (GB), as pointed out in figure 8(c). According to the dislocations theory [Hirth and Lothe 1982], the observed GB is actually a simple tilt boundary which is composed of only one set of edge dislocations. In addition, a small fraction of HCP structure with three adjacent SF layers is also observed at one end of the NW, as marked out in figure 9(c).

Figure 9 illustrates the atomic configurations of Case V with surface edge defect at strains of 0.084, 0.2 and 0.6. For convenience, we denote α_1, α_2, α_3 and α_4 as the

four edges of the NW, with the surface defect placed on edge α_1. As revealed in figure 9(a), we find atoms located around three of the NW's edges (α_2, α_3 and α_4) are experiencing a slight offset from the prefect lattice structure at the beginning of yielding. Such deformation process is highly similar as the perfect NW (figure 2(a)). This similarly is also reflected by the similar schematic of the stress-strain curves in figure 4. It should be noticed that, atoms located at edge α_1 haven't involved in such deformation.

With further deformation, we find two sets of leading partial dislocations emitted from edge α_3, where is also the opposite position of the surface defect, as shown in figure 9(b). Accompanying with the propagation of these partial dislocations to the NW's two ends, we observe a phase transformation from FCC structure to HCP structure emerged. As seen in figure 9(c), after the completion of the propagation, a large part of the NW is showing a HCP structure. Particularly, a sharp decrease of the stress-strain curve is related to this propagation progress, as highlighted in figure 4. Close examination reveals that, at the strain of 0.161, apart from the HCP structure, some middle part of the NW is having the $\{111\}$ exposure surfaces, but others still possess $\{100\}$ exposure surfaces. This observation indicates the generation of twins. Furthermore, the existence of a simple tilt GB is observed at edge α_3, as pointed out in figure 9(c).

From figure 9(d), we find the NW is fractured at the strain of 0.422, with the upper part still has a large fraction of HCP structure, but the lower part has transformed back to FCC structure. It is interested to mention that, fivefold deformation twins (FDT) are developed in the region where phase transformation happened twice (transform from FCC structure to HCP structure and then change back to FCC structure). Actually, FDT are found to have a significant effect on the mechanical properties (such as strength and toughness) of nanomaterials [Cao and Wei 2006]. Its formation is also reported by other researchers under different loading conditions for Cu NWs, e.g. Zheng et al. [Zheng, Zhang, Chen, Wang, Zhang and Wang 2008] found the formation of two conjoint FDT in Cu NWs with hollow square cross-section under bending. Jiang et al. [Jiang, Zhang, Zheng and Chen 2010] observed the FDT generated in Cu NWs under tension after pre-torsion. As shown in figure 9(d), the formation of FDT is found at the strain of 0.422. Specifically, we observe another FDT is existed at the NW's lower part, which is connected with the previous one by a common TB (TB2 in figure 9(d)). From figure 9(e), the NW is found completely fractured, with the upper part still possessing a large fraction of HCP structure.

3.2 NW with different pre-existing single internal defects

3.2.1 Deformation analysis of the NW with single internal defects

To investigate further of the defect's effect, we consider five cases by moving the surface defect into the inside of the NW. Namely, defected Cu NWs with single internal defects, and the size is $6a \times 6a \times 30a$. Although such internal defects might not exist in real materials, it is still useful for an academic analysis to enhance the understanding of the surface defect's influence at low temperature. Simulation models are shown in Figure 10, including: Case VI: with horizon defect in internal (100) plane; Case VII: with vertical defect in internal (100) plane; Case VIII: with 45^o defect in internal (100) plane; Case IX: with horizon defect in (110) plane, and Case X: with diagonal defect in (1100) plane. Different single defects are generated by removing the same amount of atoms according to different positions and orientations from the internal of the NW.

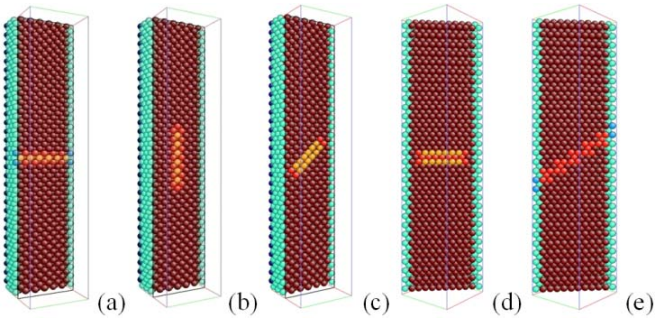

Figure 10: NWs with different pre-existing single internal defects: Case VI: horizon defect in internal (100) plane; Case VII: vertical defect in internal (100) plane; Case VIII: 45º defect in internal (100) plane; Case IX: horizon defect in (110) plane, and Case X: diagonal defect in (110) plane. All figures are sectional views.

Figure 11 shows the stress-strain curves of the five internal defected NWs, as well as the perfect NW. Again, the elastic regions of all curves are found almost coincident with each other. From the values of Young's modulus that extracted from the stress-strain curves, we find only small decrease is induced by different internal defects. Similar as NWs with single surface defects, this finding suggests Young's modulus is insensitive to the internal defect. On the contrary, an obvious decrease of yield strength is found for every internal defected NW. The most decrease is observed in Case VIII with 45˚ defect in internal (100) plane. Generally, comparing with the stress-strain curve of perfect NW, the curves of those NWs with internal

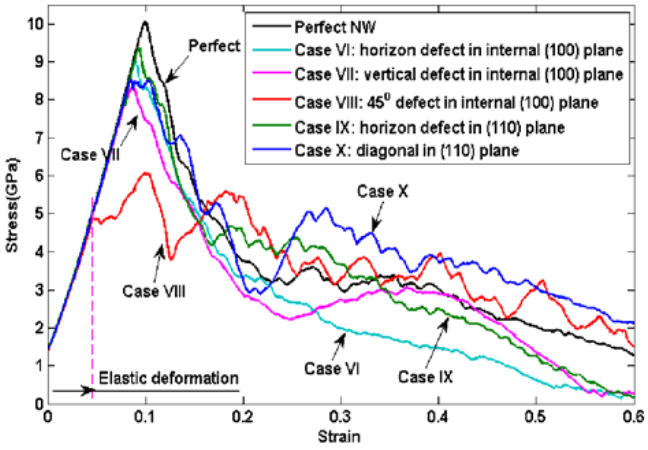

Figure 11: Stress-strain curves of NWs with different pre-existing single internal defects.

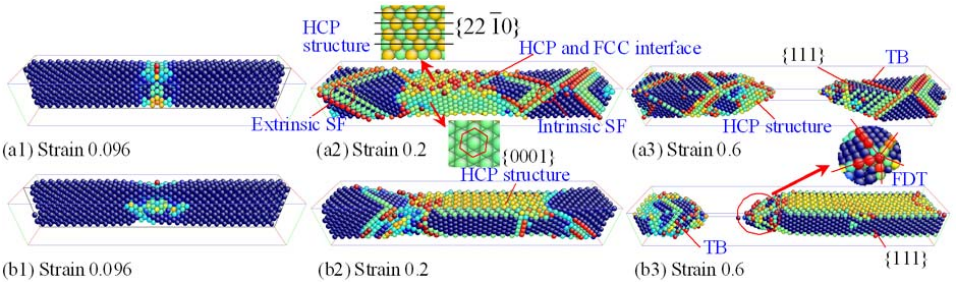

Figure 12: Atomic configurations of NWs with internal defects: (a1) (a3): Case VI at strains of 0.096, 0.2 and 0.6; (b1) (b3): Case VII at strains of 0.096, 0.2 and 0.6; Atoms with the *csp* value between 0 and 12 are visualised; Figures in the first column are sectional views.

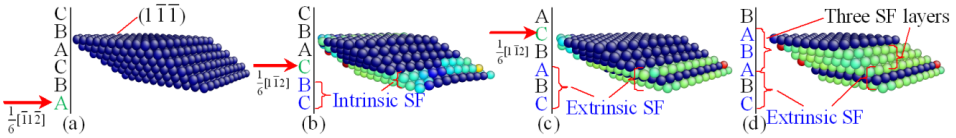

Figure 13: Formation process of a HCP structure with three SF layers: (a) perfect FCC structure; (b) intrinsic SF formation; (c) extrinsic SF formation; (d) formation of HCP structure.

defects appear more fierce fluctuations, especially for Case VIII and X.

Similar as surface defects, we observe that NWs with different internal defects have activated different deformation mechanisms. Generally, a similar deformation process is found in Case VIII, IX and X. Namely, the dominate deformation process is the nucleation and propagation of partial dislocations; partial dislocations initially emitted from the location of defect; the generation of intrinsic SF, extrinsic SF and twins. However, comparing with these three cases, Case VI and VII show a totally different deformation process as illustrated in figure 12.

For Case VI, partial dislocations are found initially emitted around the location of the internal horizon defect, as illustrated in figure 12(a1). Similar as the horizon defect at the surface in Case I, four leading partial dislocations are observed at the beginning of yielding in Case VI. With the increase of strain, the middle part of the NW is found undertaking a phase transformation process. As shown in figure 12(a2), the existences of intrinsic SF and extrinsic SF are found and the middle part of the NW has changed into the HCP structure at the strain of 0.2. The atomic configuration reveals that, the HCP structure is having the $\{0001\}$ and $\{22\bar{1}0\}$ exposure surfaces. It is interested to mention that, during the whole deformation process, only the NW's middle part has involved in. With further elongation, we find the necking phenomenon is emerged around one of the interfaces between the HCP and FCC structures. As shown in figure 12(a3), the NW is already fractured at the strain of 0.6 and a twin is developed. Particularly, comparing with figure 12(a2), the HCP structure is still existed, but with a smaller fraction.

For Case VII, partial dislocations are first generated around the defect's location at the start of yielding, as shown in figure 12(b1). In particular, two sets of intersect leading partial dislocations are observed emitted from the middle of the NW, and then propagated to the NW's two ends. This deformation process is very similar as in Case V with the surface edge defect. As illustrated in figure 12(b2), the propagation process leads to a phase transformation process, changing the original FCC structure to HCP structure. The HCP structure is the same as observed in Case VI, with the $\{0001\}$ and $\{22\bar{1}0\}$ exposure surfaces. It is interested to find that almost the entire NW has transformed into the HCP structure. With the increase of strain, necking phenomenon is observed and the NW is fractured. As shown in figure 12(b3), the HCP structure is retained and we find the rest FCC structure is having the $\{111\}$ exposure surfaces. More importantly, a FDT is developed at the fracture region as pointed out in figure 12(b3). Actually, this region is observed having the phase transformations from FCC to HCP structure and then change back to FCC structure.

3.2.2 Comparison of NWs with different pre-existing single defects

Based on the above analyses, we compared the deformation processes of all NWs with pre-existing single defects. The values of Young's modulus, yield strength and yield strain that estimated from the simulations are listed in table 1. It is seen that, for all defected NWs, Young's modulus shows very small decrease, suggesting Young's modulus is insensitive to the defect. In contrast, the presence of defect has induced a relative large decrease to yield strength, as well as yield strain.

Figure 13 compares the decrease percentage of yield strength in different cases. Generally, the surface defects are found inducing larger decrease to yield strength than the internal defects. One exception is found in the group of inclined defects, including Case III, VIII and X. In particular, Case VIII with 45° defect in internal (100) plane shows the largest decrease, with a 51.61% reduction. In the other hand, the diagonal defect in internal (110) plane only shows a decrease of 15.26%. Actually, the defects in Case III and VIII not only lie on the (100) plane, but also locate at the {111} slip plane. *The larger decrease of yield strength in Case III and VIII indicate that, defects lie on slip planes intend to introduce larger influence than other defects.*

It is observed that defects also significantly affect NWs' tensile deformation mechanisms. Table 2 summarised the deformation processes that observed in different cases. For convenience, the generations of twins, HCP structures as well as grain boundary are referred as twin, HCP and GB in table 2, respectively. PT refers to phase transformation process. It is necessary to distinguish the formation of the HCP structure in NWs with and without a phase transformation process. From the analysis in Section 3.1 and 3.2.1, the phase transformation process always takes place with the propagation of a group of intersect partial dislocations, which would leave a large fraction of the NW in a HCP structure (figures 9(c), 12(a2) and 12(b2)).

However, for the HCP structure generated without a phase transformation process, an apparent rhombus shape is observed. The formation of such structure can be well explained according to the dislocations theory [Hirth and Lothe 1982]. Figure 14 shows the formation of a HCP structure with three SF layers in Case IV. Consider the regular stacking sequence of the FCC structure as 'ABCABC' in figure 14(a), then an intrinsic SF will be generated with a $[\bar{1}1\bar{2}]/6$ displacement at the first 'A' and all successively lower planes. As represented by the arrow in figure 14(b), a $[1\bar{1}2]/6$ displacement at plane 'C' and all above planes would change the intrinsic SF into an extrinsic SF (figure 14(c)). The continuous $[1\bar{1}2]/6$ displacement above the extrinsic SF results in the generation of three adjacent SF layers (a HCP structure), as illustrated in figure 14(d). Comparing with the original stacking sequence, the

Table 1: Effects of single surface and internal defects to the tension properties

Cases	Surface defects					Internal defects					
	Perfect	I	II	III	IV	V	VI	VII	VIII	IX	X
Young's modulus	75.188	74.528	74.303	74.248	74.529	74.699	74.436	73.962	72.167	74.335	73.603
Decrease (%)	–	-0.85	-1.18	-1.25	-0.88	-0.65	-1.0	-1.63	-4.02	-1.13	-2.11
Yield strength	10.06	8.065	8.03	6.618	8.286	9.452	9.01	8.333	4.868	9.354	8.525
Decrease (%)	–	-19.83	-20.18	-34.21	-17.63	-6.04	-10.44	-17.17	-51.61	-7.02	-15.26
Yield strain	0.099	0.081	0.083	0.065	0.083	0.095	0.09	0.087	0.046	0.094	0.086
Decrease (%)	–	-18.18	-16.16	-34.34	-16.16	-4.04	-9.09	-12.12	-53.54	-5.05	-13.13

* Young's modulus & yield strength unit in *GPa*.

deformed structure shows a stacking sequence of 'CBABAB'. Analogously, the formation of the HCP structure in other cases can also be explained, e.g., in Case I, four adjacent SF layers are generated by two extrinsic SFs lying at two sides of one intrinsic SF.

Generally, according to table 2, *the pre-existing defects are observed exerting a large influence to the NW's tensile deformation mechanisms.* Comparing with the nucleation and propagation of partial dislocations dominated deformation process in perfect NW, more affluent deformation mechanisms have been activated by pre-existing defects, such deformation mechanisms including the generations of twins, HCP structure, GBs and even phase transformation. Furthermore, *the partial dislocations are first emitted from the locations of defects, which suggest that defects have played a role of dislocation source.* In addition, the necking phenomenon is also affected by different defects. Particularly, two necking areas are observed in Case VIII with 45° defect in internal (100) plane.

3.3 NW with different pre-existing surface bi-defects

According to the above discussion, the surface defect is usually exerting larger influence than the internal defect and the defect that locates at slip planes appears as the most influential one. In this section, we consider three cases with different surface bi-defects, the size of the Cu NW with $6a \times 6a \times 30a$ is considered. Simulation models are shown in figure 15, including Case XI: with two parallel 45^o surface defects; Case XII: with two crossed 45^o surface defects; Case XIII: with crossed horizon and vertical surface defects. Different models are generated by creating two surface single defects on the NWs' surface.

Figure 16(a) shows the stress-strain curves of the three surface bi-defected cases, as well as the perfect case. Similar as the single defected cases, the elastic deformation of NWs are still coincident with the perfect nanowire, indicating Young's modulus is insensitive to surface bi-defects. As seen in figure 16(a), an early yielding is observed together with a large decrease of yield strength for all three defected NWs. The comparisons of yield strength decrease between NWs with single defects and bi-defects are presented in figure 16(b). It is observed that, Case XIII with crossed horizon and vertical surface defect shows less decrease to yield strength than Case III with single 45° surface defect. This observation once again suggests that defects locating at slip planes would greatly influence NWs' properties. In general, surface bi-defects are found leading to larger decrease to yield strength than single defects and suggesting the more of defects, the larger influence will be induced.

Figure 17 shows the atomic configurations of NWs with different surface bi-defects at three strain points. Basically, all three cases appear a deformation process dominated by the nucleation and propagation of partial dislocations. Specifically, in

Table 2: Deformation mechanisms that observed in NWs with different single defects under tension

Perfect	Case I	Case II	Case III	Case IV	Case V
Intrinsic SF	Intrinsic SF	Intrinsic SF	Intrinsic SF	Intrinsic SF	Intrinsic SF
Extrinsic SF	Extrinsic SF	Extrinsic SF	Extrinsic SF	Extrinsic SF	Extrinsic SF
	Twin, HCP	Twin (rare), HCP	Twin (rare)	Twin (rare), HCP, GB	Twin, PT, GB
	Case VI	Case VII	Case VIII	Case IX	Case X
	Intrinsic SF	Intrinsic SF	Intrinsic SF	Intrinsic SF	Intrinsic SF
	Extrinsic SF	Extrinsic SF	Extrinsic SF	Extrinsic SF	Extrinsic SF
	Twin, PT	Twin, PT	Twin	Twin, HCP, GB	Twin, HCP

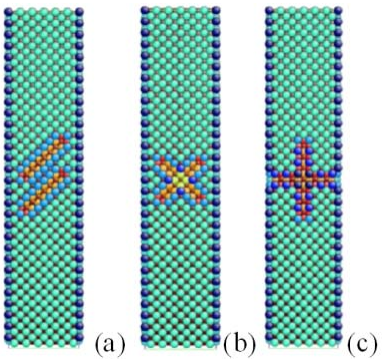

Figure 14: NWs with different pre-existing surface bi-defects: (a) Case XI: with two parallel 45^o defects; (b) Case XII: with two crossed 45^o defects; (c) Case XIII: with crossed horizon and vertical defect.

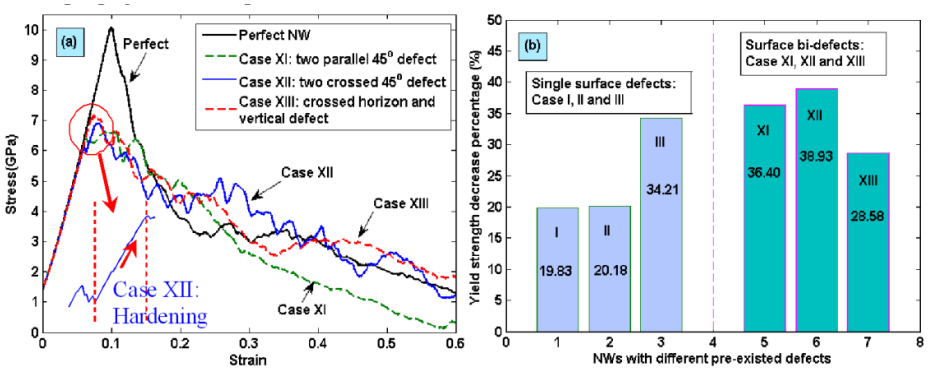

Figure 15: (a) Stress-strain curves of NWs with three different surface bi-defects; (b) Comparison of yield strength decrease by different pre-existing surface defects.

Case XI, two leading partial dislocations are initially emitted from the locations of surface defects. With further deformation, the formations of intrinsic SF, extrinsic SF and twins are observed. It is interested to mention that, one FDT is generated at the fracture region, as pointed out in figure 17(a3). However, this FDT is developed until the fracture happens, indicating it is formed due to the release of strain energy at the fracture region. In Case XII, four leading partial dislocations are found emitted from the locations of surface defects at the beginning of yielding, introducing four intersected intrinsic SFs, as shown in figure 17(b1). These intersected intrinsic SFs are observed resulting a hardening effect, as highlighted in figure 16(a), the stress is found increased until new SFs generated. At the strain of 0.6, two necking

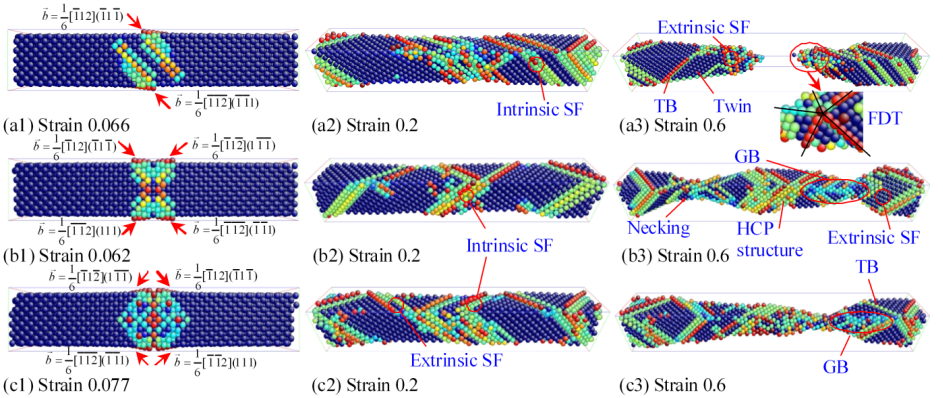

Figure 16: Atomic configurations of NWs with surface bi-defects: (a1)–(a3): Case XI at strains of 0.066, 0.2 and 0.6; (b1)–(b3): Case XII at strains of 0.062, 0.2 and 0.6; (c1)–(c3): Case XIII at strains of 0.077, 0.2 and 0.6. Atoms with the *csp* value between 0 and 12 are visualized.

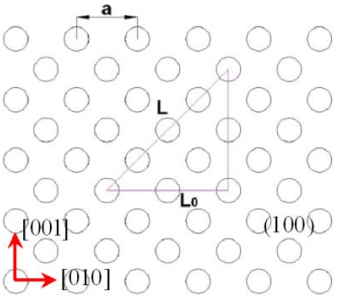

Figure 17: Schematic of a defect size. L is the defect size, a is the Cu lattice constant.

areas are found in Case XII, and a GB is formed in each necking area. Furthermore, similar HCP structure's formation process as in NWs with surface single defects is observed. From figure 17(c1), four leading partial dislocations are also found at the start of yielding in Case XIII. With the increase of strain, existences of intrinsic SF and extrinsic SF are observed. At the strain of 0.6, a GB is developed at the necking area. In all, comparing with the deformation of perfect NW, an obvious influence to the deformation mechanism is induced due to the surface bi-defects.

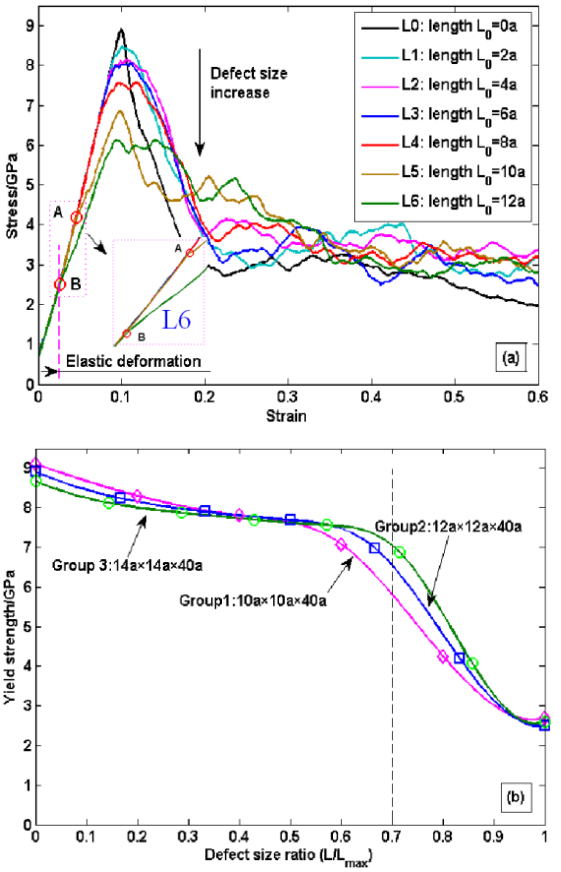

Figure 18: (a) Stress-strain curves of NWs in Group 2; (b) Defect size effect to yield strength.

3.4 Influence of defect sizes

The study of the defect's size effect has also been carried out. In order to get sufficient results, we consider three groups of simulations, including: Group 1: with the NW's size of $10a\times10a\times40a$; Group 2: with the NW's size of $12a\times12a\times40a$; Group 3: with the NW's size of $14a\times14a\times40a$. As defects lying on slip planes intend to induce larger influence, thus, in this section, surface 45^o defect with different sizes will be employed in each group. For convenience, the size of a defect is defined as $L = L_0\sqrt{2}$, as illustrated in figure 18, with the defect size ratio r refer as $r = L/L_{\max}$, where $L_{\max}$ is the maximum size of the surface 45^o defect for a given NW. For example, in Group 2, the maximum size is $12\sqrt{2}a$ (when defect crosses

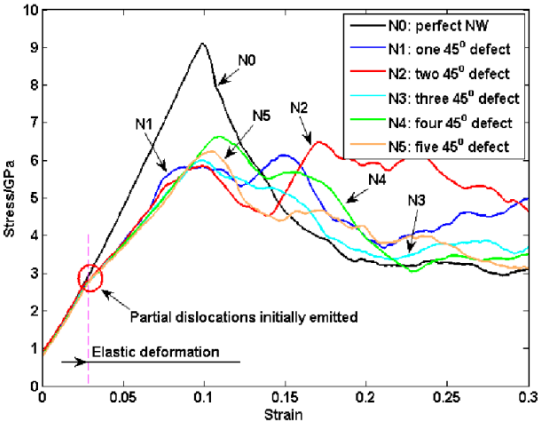

Figure 19: Stress-strain curves of NWs with different quantities of pre-existing surface 45° defect.

over the whole surface), and the defect sizes including: 0, $2\sqrt{2}a$, $4\sqrt{2}a$, $6\sqrt{2}a$, $8\sqrt{2}a$, $10\sqrt{2}a$ and $12\sqrt{2}a$ are considered.

Because of the similarity of the stress-strain curves in each group, only curves of Group 2 are presented in figure 19(a). In general, NWs with different sizes of defects are found almost having a similar elastic deformation region as pointed out in figure 19(a). It is observed that, in Case L5 and Case L6, another linear part of the stress-strain curves with a smaller slope is developed, which has been taken as elastic deformation in the beginning. Actually, the atomic configurations of these two cases suggest that partial dislocations are emitted from the locations of defects once the stress-strain curves deviated from the first linear part (as marked out by the 'o' mark in figure 19(a)), which indicates the beginning of yielding. Therefore, the results of Group 2 have once again proved that, Young's modulus is insensitive to the surface defect, and yield strength and yield strain have received large decrease due to the surface defect. Same results are also seen in Group 1 and Group 3.

Figure 19(b) shows the defect size effect to yield strength. Apparently, the curves for these three groups appear very similar to each other. Accompanying with the increasing defect size ratio, larger influence is observed. In particular, for Group 2, yield strength at the defect size ratio of 1.0 is estimated about 2.501 *GPa*, which is less than one third of the perfect NW with 8.906 *GPa*. In all, from figure 19(b), we find that yield strength shows a gentle decrease until the size ratio is around 0.7. After that, a sharp reduction is observed in all three groups. It could be concluded that, the longer of the defect, the larger influence to yield strength and yield strain will be induced.

3.5 Influence of defect quantities

Discussions are based on simulations of NWs with different quantities of pre-existing surface 45° defect. It should be noticed here that NWs with many surface defects might not realistic. However, for an academic analysis, this investigation would shed light on our concern: does Young's modulus change if a NW possesses a large number of defects? Therefore, a discussion will be presented in this section to investigate the effect of defect quantity. MD simulations are carried out for a group of NWs with the same size as $10a \times 10a \times 40a$. Different quantities including one to five parallel surface 45° defects are considered. Each surface 45° defect has the largest size as $10\sqrt{2}a$ (defect crosses over the whole surface).

Figure 20 shows the stress-strain curves of NWs with different quantities of 45° defects. Generally, all stress-strain curves of defected NWs are showing an almost coincident linear part at the early stage of deformation, which are observed deviating to another linear part with a smaller slope at an approximate same strain point (around strain 0.03). More importantly, according to the atomic configurations, we find partial dislocations would emit from the locations of surface defects once the stress-strain curve deviates from the original linear part. Therefore, based on the yield strength definition in section 2.1, we only consider the first linear part as elastic deformation. Hence, Young's modulus that extracted from the first linear part would be almost the same with the perfect NW. This observation has once again proved that Young's modulus is insensitive to pre-existing defects, even for multiple defects.

4 Conclusions

In summary, comprehensive molecular dynamics (MD) simulations have been carried out to explore the tensile deformation properties for Cu NWs with different pre-existing defects. Different styles of pre-existing defects including single surface defects, surface bi-defects and single internal defects have been considered. The influences of the defect size and quantity have also been investigated. Conclusions are drawn as below:

1. Young's modulus is found insensitive to different styles of pre-existing defects, and also the defect size; Due to the presences of defects, yield strength and yield strain appear a large decrease;

2. Pre-existing defects have played a role of dislocation sources, partial dislocations are first emitted from the locations of defects. Further, the necking locations have been also affected by different defects;

3. Pre-exist defects have exerted a large influence to NWs' tensile deformation processes. More affluent deformation mechanisms, including the generations of twins, fivefold deformation twins, grain boundaries, HCP structure and even phase transformation have been triggered by defects;

4. Generally, the surface defect tends to induce bigger decrease to yield strength than internal defect;

5. Defect that lies on slip planes will result larger influence than other defects, such as the 45° defect in (100) plane;

6. From the investigation of pre-existing surface defects with different sizes and quantities, it has found that the more or longer of the defects, the larger influence is observed.

Conclusively, this study provides a fundamental understanding of Cu NW's properties when there are defects presented.

Appendix: Simulation models summary

1. Perfect NW, size of $6a \times 6a \times 30a$ (section 2.2);

2. Perfect NW with different cross-sectional sizes, including: $4a$, $6a$, $8a$, $10a$, $12a$, $14a$ and the length of all NWs as $30a$ (section 2.2);

3. NW with pre-existing single surface defect, size of $6a \times 6a \times 30a$ (section 3.1, figure 3);

    - Case I: with a surface horizon defect;
    - Case II: with a surface vertical defect;
    - Case III: with a surface 45^o defect;
    - Case IV: with a surface corner defect;
    - Case V: with a surface edge defect.

4. NW with pre-existing single internal defect, size of $6a \times 6a \times 30a$ (section 3.2.1, figure 10);

    - Case VI: with horizon defect in the internal (100) plane;
    - Case VII: with vertical defect in internal (100) plane;
    - Case VIII: with 45^o defect in internal (100) plane
    - Case IX: with horizon defect in (110) plane;

- Case X: with diagonal defect in (110) plane.

5. NW with pre-existing surface bi-defects, size of $6a\times6a\times30a$ (section 3.3, figure 15);
   - Case XI: with two parallel 45^o surface defects;
   - Case XII: with two crossed 45^o surface defects;
   - Case XIII: with crossed horizon and vertical surface defects.
6. NW with different sizes of surface single 45^o defect (section 3.4, Table 3)
7. NW with different quantities of surface 45^o defect, including one, two, three, four and five parallel defects, the size of the model is $10a\times10a\times40a$. Each 45^o defect crosses over the whole surface with the largest size as $10\sqrt{2}a$ (section 3.5).

References

Cao, A.; Wei, Y. (2006): Atomistic simulations of the mechanical behavior of fivefold twinned nanowires. *Phys. Rev. B*, *vol. 74*, pp. 214108.

Cao, A.; Wei, Y.; Mao, S. (2007): Deformation mechanisms of face-centered-cubic metal nanowires with twin boundaries. *Appllied Physical Letters*, *vol. 90*, pp. 151909.

Cao, A.J.; Wei, Y.G. (2006): Formation of fivefold deformation twins in nanocrystalline face-centered-cubic copper based on molecular dynamics simulations. *Apllied Physical Letters*, *vol. 89*, pp. 041919-041913.

Chan, W.K.; Luo, M.; Zhang, T.Y. (2008): Molecular dynamics simulations of four-point bending tests on SiC nanowires. *Scripta Mater.*, *vol. 59*, pp. 692-695.

Chang, W.J. (2003): Molecular-dynamics study of mechanical properties of nanoscale copper with vacancies under static and cyclic loading. *Microelectron. Eng.*, *vol. 65*, pp. 239-246.

Chen, C.; Zhu, J. (2007): Bending strength and flexibility of ZnO nanowires. *Appl. Phys. Lett.*, *vol. 90*, pp. 043105.

Chen, M.J.; Xiao, G.B.; Chen, J.X.; Wu, C.Y. (2010): Research on the influence of machining introduced sub-surface defects and residue stress upon the mechanical properties of single crystal copper. *SCIENCE CHINA Technological Sciences*, *vol. 53*, pp. 3161-3167.

Da Silva, E.; Da Silva, A.J.R.; Fazzio, A. (2001): How do gold nanowires break? *Phys. Rev. Lett.*, *vol. 87*, pp. 256102.

Table 3: NW with different sizes of surface single 45^o defect

Case	L0	L1	L2	L3	L4	L5	L6	L7
Group 1: $10a\times10a\times40a$	0	$2\sqrt{2}a$	$4\sqrt{2}a$	$6\sqrt{2}a$	$8\sqrt{2}a$	$10\sqrt{2}a$		
Group 2: $12a\times12a\times40a$	0	$2\sqrt{2}a$	$4\sqrt{2}a$	$6\sqrt{2}a$	$8\sqrt{2}a$	$10\sqrt{2}a$	$12\sqrt{2}a$	
Group 3: $14a\times14a\times40a$	0	$2\sqrt{2}a$	$4\sqrt{2}a$	$6\sqrt{2}a$	$8\sqrt{2}a$	$10\sqrt{2}a$	$12\sqrt{2}a$	$14\sqrt{2}a$

*a is the Cu lattice constant, equals 3.615 $\mathring{A}$.

Daw, M.; Baskes, M. (1984): Embedded-atom method: Derivation and application to impurities, surfaces, and other defects in metals. *Physical Review B*, *vol. 29*, pp. 6443-6453.

Deng, C.; Sansoz, F. (2009): Enabling Ultrahigh Plastic Flow and Work Hardening in Twinned Gold Nanowires. *Nano Lett.*, *vol. 9*, pp. 1517-1522.

Deng, C.; Sansoz, F. (2009): Fundamental differences in the plasticity of periodically twinned nanowires in Au, Ag, Al, Cu, Pb and Ni. *Acta Mater.*, *vol. 57*, pp. 6090-6101.

Diao, J.; Gall, K. (2004): Atomistic simulation of the structure and elastic properties of gold nanowires. *J. Mech. Phys. Solids*, *vol. 52*, pp. 1935-1962.

Diao, J.; Gall, K.; Dunn, M.; Zimmerman, J. (2006): Atomistic simulations of the yielding of gold nanowires. *Acta Mater.*, *vol. 54*, pp. 643-653.

Diao, J.; Gall, K.; Dunn, M.L. (2003): Surface-stress-induced phase transformation in metal nanowires. *Nat. Mater.*, *vol. 2*, pp. 656-660.

Diao, J.; Gall, K.; Dunn, M.L. (2004): Surface stress driven reorientation of gold nanowires. *Phys. Rev. B*, *vol. 70*, pp. 075413.

Doyama, M. (1995): Simulation of plastic deformation of small iron and copper single crystals. *Nuclear Instruments and Methods in Physics Research Section B: Beam Interactions with Materials and Atoms*, *vol. 102*, pp. 107-112.

Ekinci, K.; Roukes, M. (2005): Nanoelectromechanical systems. *Rev. Sci. Instrum.*, *vol. 76*, pp. 061101.

Foiles, S.; Baskes, M.; Daw, M. (1986): Embedded-atom-method functions for the fcc metals Cu, Ag, Au, Ni, Pd, Pt, and their alloys. *Phys. Rev. B*, *vol. 33*, pp. 7983-7991.

Gall, K.; Diao, J.; Dunn, M.L. (2004): The strength of gold nanowires. *Nano Lett.*, *vol. 4*, pp. 2431-2436.

Ghoniem, N.M.; Cho, K. (2002): The emerging role of multiscale modeling in nano-and micro-mechanics of materials. *Computer Modeling in Engineering and Sciences*, *vol. 3*, pp. 147-174.

He, J.; Lilley, C. (2008): Surface stress effect on bending resonance of nanowires with different boundary conditions. *Appllied Physical Letters*, *vol. 93*, pp. 263108.

Heidelberg, A.; Ngo, L.T.; Wu, B.; Phillips, M.A.; Sharma, S.; Kamins, T.I.; Sader, J.E.; Boland, J.J. (2006): A generalized description of the elastic properties of nanowires. *Nano Lett.*, *vol. 6*, pp. 1101-1106.

Higgins, D.A.; Bout, D.a.V.; Kerimo, J.; Barbara, P.F. (1996): Polarization-modulation near-field scanning optical microscopy of mesostructured materials.

The Journal of Physical Chemistry, *vol. 100*, pp. 13794-13803.

Hirth, J.P.; Lothe, J. (1982): Theory of dislocations. *John Wiley and Sons, Inc., 1982*, *vol.*, pp. 857.

Hoffmann, S.; Utke, I.; Moser, B.; Michler, J.; Christiansen, S.H.; Schmidt, V.; Senz, S.; Werner, P.; Gösele, U.; Ballif, C. (2006): Measurement of the bending strength of vapor-liquid-solid grown silicon nanowires. *Nano Lett.*, *vol. 6*, pp. 622-625.

Hoover, W.G. (1985): Canonical dynamics: Equilibrium phase-space distributions. *Phys. Rev. A*, *vol. 31*, pp. 1695-1697.

Huang, D.; Zhang, Q.; Guo, Y. (2006): Molecular dynamics simulation of axial tension process of ¦Á-Fe and Ni nano wires. *Ordnance material science and engineering*, *vol. 29*, pp. 12-15.

Husain, A.; Hone, J.; Postma, H.W.C.; Huang, X.; Drake, T.; Barbic, M.; Scherer, A.; Roukes, M. (2003): Nanowire-based very-high-frequency electromechanical resonator. *Appl. Phys. Lett.*, *vol. 83*, pp. 1240.

Ikeda, H.; Qi, Y.; agin, T.; Samwer, K.; Johnson, W.L.; Goddard, W.A. (1999): Strain Rate Induced Amorphization in Metallic Nanowires. *Phys. Rev. Lett.*, *vol. 82*, pp. 2900.

Ishigami, M.; Choi, H.; Aloni, S.; Louie, S.; Cohen, M.; Zettl, A. (2004): Identifying defects in nanoscale materials. *Phys. Rev. Lett.*, *vol. 93*, pp. 196803.

Ji, C.; Park, H. (2007): The coupled effects of geometry and surface orientation on the mechanical properties of metal nanowires. *Nanotechnology*, *vol. 18*, pp. 305704.

Jiang, S.; Zhang, H.; Zheng, Y.; Chen, Z. (2009): Atomistic study of the mechanical response of copper nanowires under torsion. *J. Phys. D: Appl. Phys.*, *vol. 42*, pp. 135408.

Jiang, S.; Zhang, H.; Zheng, Y.; Chen, Z. (2010): Loading path effect on the mechanical behaviour and fivefold twinning of copper nanowires. *J. Phys. D: Appl. Phys.*, *vol. 43*, pp. 335402.

Jiang, W.; Batra, R. (2009): Molecular statics simulations of buckling and yielding of gold nanowires deformed in axial compression. *Acta Mater.*, *vol. 57*, pp. 4921-4932.

Kelchner, C.; Plimpton, S.; Hamilton, J. (1998): Dislocation nucleation and defect structure during surface indentation. *Phys. Rev. B*, *vol. 58*, pp. 11085-11088.

Koh, A.; Lee, H. (2006): Shock-induced localized amorphization in metallic nanorods with strain-rate-dependent characteristics. *Nano Lett.*, *vol. 6*, pp. 2260-2267.

Koh, S.; Lee, H. (2006): Molecular dynamics simulation of size and strain rate dependent mechanical response of FCC metallic nanowires. *Nanotechnology*, *vol. 17*, pp. 3451.

Koh, S.; Lee, H.; Lu, C.; Cheng, Q. (2005): Molecular dynamics simulation of a solid platinum nanowire under uniaxial tensile strain: Temperature and strain-rate effects. *Phys. Rev. B*, *vol. 72*, pp. 085414.

Kuramoto, E.; Ohsawa, K.; Tsutsumi, T. (2002): Computer simulation of fundamental behaviors of point defects, clusters and interaction with dislocations in Fe and Ni. *CMES: Computer Modeling in Engineering and Sciences*, *vol. 3*, pp. 193-200.

Li, M.; Mayer, T.S.; Sioss, J.A.; Keating, C.D.; Bhiladvala, R.B. (2007): Template-grown metal nanowires as resonators: performance and characterization of dissipative and elastic properties. *Nano Lett.*, *vol. 7*, pp. 3281-3284.

Liang, W.; Zhou, M. (2003): Size and strain rate effects in tensile deformation of Cu nanowires. *Nanotechnology*, *vol. 2*, pp. 452-455.

Liang, W.; Zhou, M. (2004): Response of copper nanowires in dynamic tensile deformation. *Proceedings of the Institution of Mechanical Engineers, Part C: Journal of Mechanical Engineering Science*, *vol. 218*, pp. 599-606.

Liang, W.; Zhou, M.; Ke, F. (2005): Shape Memory Effect in Cu Nanowires. *Nano Lett.*, *vol. 5*, pp. 2039-2043.

Mcdowell, M.; Leach, A.; Gall, K. (2008): Bending and tensile deformation of metallic nanowires. *Modell. Simul. Mater. Sci. Eng.*, *vol. 16*, pp. 045003.

Mishin, Y.; Mehl, M.; Papaconstantopoulos, D.; Voter, A.; Kress, J. (2001): Structural stability and lattice defects in copper: Ab initio, tight-binding, and embedded-atom calculations. *Phys. Rev. B*, *vol. 63*, pp. 224106.

Ni, H.; Li, X. (2006): Young's modulus of ZnO nanobelts measured using atomic force microscopy and nanoindentation techniques. *Nanotechnology*, *vol. 17*, pp. 3591.

Nosé, S. (1984): A unified formulation of the constant temperature molecular dynamics methods. *J. Chem. Phys.*, *vol. 81*, pp. 511.

Olsson, P.a.T.; Park, H.S. (2011): Atomistic study of the buckling of gold nanowires. *Acta Mater.*, *vol. 59*, pp. 3883–3894.

Park, H.; Gall, K.; Zimmerman, J. (2006): Deformation of FCC nanowires by twinning and slip. *J. Mech. Phys. Solids*, *vol. 54*, pp. 1862-1881.

Park, H.; Klein, P. (2007): Surface Cauchy-Born analysis of surface stress effects on metallic nanowires. *Phys. Rev. B*, *vol. 75*, pp. 85408.

Park, H.; Klein, P.; Wagner, G. (2006): A surface Cauchy-Born model for nanoscale materials. *Int. J. Numer. Meth. Engng*, *vol. 68*, pp. 1072-1095.

Park, H.S.; Gall, K.; Zimmerman, J.A. (2005): Shape memory and pseudoelasticity in metal nanowires. *Phys. Rev. Lett.*, *vol. 95*, pp. 255504.

Park, H.S.; Ji, C. (2006): On the thermomechanical deformation of silver shape memory nanowires. *Acta Mater.*, *vol. 54*, pp. 2645-2654.

Park, H.S.; Zimmerman, J.A. (2005): Modeling inelasticity and failure in gold nanowires. *Phys. Rev. B*, *vol. 72*, pp. 54106.

Plimpton, S. (1995): Fast parallel algorithms for short-range molecular dynamics. *J. Comput. Phys.*, *vol. 117*, pp. 1-19.

Plimpton, S.; Crozier, P.; Thompson, A. 2007. LAMMPS Molecular Dynamics Simulator Sandia National Lab.

Rugar, D.; Budakian, R.; Mamin, H.; Chui, B. (2004): Single spin detection by magnetic resonance force microscopy. *Nature*, *vol. 430*, pp. 329-332.

Sansoz, F.; Huang, H.; Warner, D.H. (2008): An atomistic perspective on twinning phenomena in nano-enhanced fcc metals. *JOM Journal of the Minerals, Metals and Materials Society*, *vol. 60*, pp. 79-84.

Sarkar, J.; Khan, G.; Basumallick, A. (2007): Nanowires: properties, applications and synthesis via porous anodic aluminium oxide template. *Bull. Mater. Sci.*, *vol. 30*, pp. 271-290.

Shim, H.W.; Zhou, L.; Huang, H.; Cale, T.S. (2005): Nanoplate elasticity under surface reconstruction. *Appl. Phys. Lett.*, *vol. 86*, pp. 151912.

Streitz, F.; Cammarata, R.; Sieradzki, K. (1994): Surface-stress effects on elastic properties. I. Thin metal films. *Phys. Rev. B*, *vol. 49*, pp. 10699.

Sutrakar, V.K.; Mahapatra, D.R. (2009): Coupled effect of size, strain rate, and temperature on the shape memory of a pentagonal Cu nanowire. *Nanotechnology*, *vol. 20*, pp. 045701.

Tyagi, S.; Lee, J.; Buxton, G.; Balazs, A. (2004): Using nanocomposite coatings to heal surface defects. *Macromolecules*, *vol. 37*, pp. 9160-9168.

Van Swygenhoven, H.; Derlet, P.M. (2008). Chapter 81 Atomistic Simulations of Dislocations in FCC Metallic Nanocrystalline Materials. In *Dislocations in Solids*, H. JOHN Ed. Elsevier, 1-42.

Wan, J.; Fan, Y.; Gong, D.; Shen, S.; Fan, X. (1999): Surface relaxation and stress of fcc metals: Cu, Ag, Au, Ni, Pd, Pt, Al and Pb. *Modell. Simul. Mater. Sci. Eng.*, *vol. 7*, pp. 189.

Wang, G.F.; Feng, X.Q. (2007): Effects of surface elasticity and residual surface

tension on the natural frequency of microbeams. *Appllied Physical Letters*, *vol. 90*, pp. 231904.

Weinberger, C.; Cai, W. (2010): Orientation-Dependent Plasticity in Metal Nanowires under Torsion: Twist Boundary Formation and Eshelby Twist. *Nano Lett.*, *vol. 10*, pp. 139-142.

Wu, B.; Heidelberg, A.; Boland, J.J.; Sader, J.E.; Sun, X.M.; Li, Y.D. (2006): Microstructure-hardened silver nanowires. *Nano Lett.*, *vol. 6*, pp. 468-472.

Wu, H. (2006): Molecular dynamics study on mechanics of metal nanowire. *Mechanics Research Communications*, *vol. 33*, pp. 9-16.

Xia, Y.; Yang, P.; Sun, Y.; Wu, Y.; Mayers, B.; Gates, B.; Yin, Y.; Kim, F.; Yan, H. (2003): One-dimensional nanostructures: synthesis, characterization, and applications. *Adv. Mater.*, *vol. 15*, pp. 353-389.

Yan, Y.; Zhang, J.; Sun, T.; Fei, W.; Liang, Y.; Dong, S. (2008): Nanobending of nanowires: A molecular dynamics study. *Appl. Phys. Lett.*, *vol. 93*, pp. 241901.

Yang, Y.; Callegari, C.; Feng, X.; Ekinci, K.; Roukes, M. (2006): Zeptogram-scale nanomechanical mass sensing. *Nano Lett.*, *vol. 6*, pp. 583-586.

Yue, Y.; Liu, P.; Zhang, Z.; Han, X.D.; Ma, E. (2011): Approaching the Theoretical Elastic Strain Limit in Copper Nanowires. *Nano Lett.*, *vol.*, pp.

Zhan, H.F.; Gu, Y.T.; Yan, C.; Feng, X.Q.; Yarlagadda, P. (2011): Numerical exploration of plastic deformation mechanisms of copper nanowires with surface defects. *Comput. Mater. Sci.*, *vol. 50*, pp. 3425-3430.

Zhan, H.F.; Gu, Y.T.; Yarlagadda, P. (2011): Advanced numerical characterization of mono-crystalline copper with defects. *Adv. Sci. Lett.*, *vol. 4*, pp. 1293-1301.

Zhang, Y.; Huang, H. (2009): Do Twin Boundaries Always Strengthen Metal Nanowires? *Nanoscale research letters*, *vol. 4*, pp. 34-38.

Zhang, Y.; Huang, H.; Atluri, S.N. (2008): Strength Asymmetry of Twinned Copper Nanowires under Tension and Compression. *CMES: Computer Modeling in Engineering & Sciences*, *vol. 35*, pp. 215-226.

Zhao, K.J.; Chen, C.Q.; Shen, Y.P.; Lu, T.J. (2009): Molecular dynamics study on the nano-void growth in face-centered cubic single crystal copper. *Comput. Mater. Sci.*, *vol. 46*, pp. 749-754.

Zheng, Y.; Zhang, H.; Chen, Z.; Wang, L.; Zhang, Z.; Wang, J. (2008): Formation of two conjoint fivefold deformation twins in copper nanowires with molecular dynamics simulation. *Appl. Phys. Lett.*, *vol. 92*, pp. 041913.